SURGICAL ROBOTS

A minimally invasive robotic spinal surgical system for anterior lumbar nerve decompression

Qingxiang Zhao[1]†, Xiandi Wang[2]†, Xin Zhong[1], Runfeng Zhu[1], Peizhi Zhou[3], Dan Pu[2], Baitao Lin[1], Tao Li[1], Shiyuan Sui[1], Haonan Zhou[1], Yuxi Cheng[1], Hao Zheng[4], Henry K. Chu[4], Jiancheng Zeng[5]*, Kang Li[1,6]*

Lumbar degenerative diseases, primarily caused by pathological tissues compressing spinal nerves, typically necessitate surgical intervention—specifically lumbar nerve decompression—to alleviate pain. Although the anterior decompression approach demonstrates notable advantages, such as reduced bleeding and shorter postoperative hospitalization stays, compared with the conventional posterior approach, patients may still experience incomplete decompression because of various instrumental shortcomings, including restricted visibility and insufficiency of distal dexterity. In this study, we present a robotic surgical system for minimally invasive anterior lumbar nerve decompression, which comprises three slender robotic arms (2 millimeters in outer diameter) with high dexterity (18 degrees of freedom), facilitating effective navigation through the narrow intervertebral disc space to reach the posterior area. Each robot arm is based on concentric push-pull robot structure, forming three robotized instruments: an endoscope for visualization, a laser optical fiber for hemostasis and resection, and a gripper for tissue manipulation. These components are integrated through the hollow lumen of a slender trocar, and multi-instrument coordination enables effective decompression procedure with wide view. System performance was first validated using a three-dimensional–printed vertebral phantom model to confirm accessibility to bilateral articular processes. Subsequently, in vivo animal experiment and human cadaver tests were conducted to further demonstrate the full capabilities in performing minimally invasive lumbar nerve decompression. This study demonstrates the potential of the robotic system to facilitate surgical procedures in narrow, confined, and tortuous anatomical spaces, addressing the key limitations of conventional instruments in anterior lumbar nerve decompression.

INTRODUCTION

Lumbar degenerative diseases (*1*), primarily caused by aging and sedentary lifestyles, impose substantial lower back and leg pain on affected patients. These conditions are no longer confined to the geriatric population but are increasingly prevalent among young adults. Studies have reported ~266 million annual cases of lower back pain attributed to degenerative spine diseases (*2*), with projections suggesting that around 890 million individuals will be affected globally by 2050 (*3*). The core pathogenic mechanism involves the compression of spinal canal nerves by degenerative structures (fig. S1A), including disc herniation, osteophyte formation, and ligamentum flavum hypertrophy (fig. S1B) (*4*). Consequently, surgical decompression (resection of these degenerative structures) and spinal fusion [placement of an interbody fusion cage (fig. S1C)] have become important clinical procedures to alleviate symptoms and restore spinal stability (*5*–*8*). Nevertheless, current surgical approaches either necessitate extensive incisions or result in incomplete decompression because of the inherent limitations of available instruments. To address these challenges, we developed a robotic system that leverages the minimally invasive and low-hemorrhage benefits of the anterior approach. By using slender, highly dexterous robotic arms equipped with integrated surgical tools, our objective is to facilitate direct, precise, and complete lumbar nerve decompression through a minimally invasive corridor.

Posterior and anterior surgical techniques both achieve decompression and fusion, but they have weaknesses. The traditional posterior approach is widely used to directly resect degenerative spinal tissues located in the posterior spinal area (*9*). In this procedure, the patient's body is in a prone position, and the surgeon makes an incision to dissect the skin and paraspinal muscles for adequate vertebral exposure (fig. S1D). Direct decompression is achieved by resecting the pathological posterior laminae and articular processes, thereby relieving lumbar nerve compression. Although the posterior decompression approach achieves greater than 85% symptomatic relief (*10*), it is concurrently associated with intraoperative blood loss of 300 to 500 ml (*11*) and a 21.6% risk of complications (*12*, *13*). In contrast, the anterior approach (*14*) uses a small lumbar incision to access the target vertebra through a retroperitoneal anatomical corridor (fig. S1E), followed by interbody fusion cage implantation. Oblique lateral interbody fusion (OLIF) (*15*) is a prominent anterior technique characterized by minimal muscle damage and reduced intraoperative blood loss, which is typically around 30 ml (*16*). Despite these advantages, clinical evidence shows that OLIF provides only moderate efficacy (65 to 78%) for central canal stenosis and remains ineffective against posterior pathologies, such as facet joint hypertrophy (*17*). This limitation results in a 32.4% postoperative residual symptom rate, primarily because of unaddressed posterior compression (*18*). As illustrated in fig. S1F, the inherently rigid and straight configuration of conventional surgical instruments severely constrains the operational workspace and visual field necessary for the precise resection of degenerative structures. Consequently, surgeons rely on interbody fusion cage implantation to expand space for the compressed nerves and treat spondylolisthesis. However, this indirect technique fails to physically resect posterior degenerative tissues, such as the superior articular processes, thereby resulting in incomplete decompression.

[1]West China Biomedical Big Data Center, West China Hospital, Sichuan University, Chengdu 610041, China. [2]Medical Simulation Center, West China Hospital, Sichuan University, Chengdu 610041, China. [3]Department of Neurosurgery, West China Hospital, Sichuan University, Chengdu 610041, China. [4]Department of Mechanical Engineering, Hong Kong Polytechnic University, Kowloon, Hong Kong SAR. [5]Department of Orthopedics, West China Hospital, Sichuan University, Chengdu 610041, China. [6]Sichuan University–Pittsburgh Institute, Sichuan University, Chengdu 610041, China.
†These authors contributed equally to this work.
*Corresponding author. Email: tomzeng5@163.com (J.Z.); likang@wchscu.cn (K.L.)

In modern spinal surgery, conventional instruments remain rigid, straight, and often oversized for accessing the constricted posterior region (*19*), which underscores the urgent clinical necessity for advanced instrumentation to enhance OLIF decompression outcome.

Minimal invasiveness is an important unmet need in modern surgery, where the inherent benefits of anterior decompression have catalyzed the development of advanced instrumentation to enhance visualization and maneuverability in confined operative spaces. In spine surgery, angled endoscopes (*20*, *21*), microscopes (*22*), and headlight-loupe combinations (*23*) have been clinically used to augment visual clarity. However, achieving comprehensive visualization remains challenging despite high-resolution imaging, primarily because of limited distal dexterity for navigating tortuous anatomical routes (*24*) and visual occlusion resulting from venous plexus hemorrhage (*25*). An estimated 46.2 to 58.7% of the posterior canal wall remains obscured in conventional practice (*26*). A miniaturized endoscopic camera integrated into a steerable robotic arm, analogous to the Da Vinci SP system (*27*, *28*), represents a promising solution to these constraints, but the size is not suitable for this procedure. To effectively support OLIF, robotic instruments must fulfill three fundamental requirements: reachability, visibility, and maneuverability in the narrow spinal anatomy. First, slenderness is an absolute prerequisite, given that the intervertebral disc space typically measures only 8 to 13 mm in height (*29*). This narrow corridor is the only path through which instruments can navigate to access the posterior area. Furthermore, because surgical resection generally necessitates the simultaneous deployment of multiple tools, such as a gripper for tissue manipulation and a rongeur for resection (*30*), only miniaturized instruments can operate effectively in this confined anatomy. Second, distal dexterity is essential, given that the superior and inferior articular processes are located at the posterior side of the spinal canal. This anatomical positioning makes it exceedingly difficult for conventional straight instruments to navigate the required tortuous routes. Last, the steerable segments of the instruments must provide enough rigidity to effectively retract and strip elastic spinal tissues (*31*).

The structural design of these instruments is thus critical. Researchers have developed continuum robots for surgical applications, including tendon-driven articulated linkage robots (*28*, *32*) (8-mm diameter, single-segment bending) and fluid-driven flexible manipulators (*33*–*35*), but these face stiffness and dexterity insufficiency. Furthermore, electroactive polymers (*36*) and magnetically driven robots (*37*) typically require bulky external systems for actuation. One promising architecture is the concentric tube robot (CTR), which features a hollow lumen and a slender robotic body (*38*–*40*). Nevertheless, CTRs are predominantly fabricated from nickel-titanium (nitinol) alloys, which have a Young's modulus of only ~40 to 75 GPa (*41*). In comparison, stainless steel offers a higher Young's modulus of ~200 GPa. The lower modulus of nitinol-based structures can result in undesirable rigidity (insufficient stiffness) when interacting with resistant spinal tissues. To address these limitations, we integrated the concentric push-pull robot (CPPR) architecture (*42*, *43*) to develop a robotic platform that we call MicroSpine for minimally invasive lumbar nerve decompression (fig. S1G). Inspired by the configuration of single-port, multiarm surgical robots, similar to the triple-arm system proposed by Bruns *et al.* (*44*) for transnasal surgery, the MicroSpine system uses CPPR-based instruments featuring specialized tenon-mortise slits. This work leverages the unique advantages of these instruments, which are characterized by slenderness, a hollow lumen, relatively high structural stiffness, and notable bending curvature.

Compared with manual instrument manipulation by surgeons at the bedside, robot-assisted surgery provides distinct clinical benefits, including the simultaneous control of multiple instruments, effective tremor elimination, digitized and traceable procedural data, and reduced radiation exposure for the surgical team (*45*–*47*). Notable progress has been made in spinal robotic systems, including precision intraoperative navigation [Renaissance, Mazor Robotics (*48*)], real-time imaging [ExcelsiusGPS, Globus Medical (*49*)], and lumbar facet fixation systems [CAVUX FFS-LX, Providence Medical Technology (*50*)]. The instruments on these systems either are straight or have limited distal steerability, making them inadequate for traversing the complex posterior spinal anatomy and performing complete decompression procedure via an oblique lumbar route.

In this work, we designed slender, highly dexterous CPPR-based instruments to navigate and manipulate in the confined and complex lumbar vertebral anatomy. To form the steerable and passive compliant segments, we manufactured tenon-mortise slits and "I"-shaped slits on hollow steel tubes, respectively. Each robotic instrument features a 2-mm outer diameter (OD) and 0.9-mm inner diameter (ID), providing a hollow lumen for tip tool integration. With 6 degrees of freedom (DoF) and a dual-segment architecture, the instruments facilitate flexible resection of degenerative tissues while maintaining a comprehensive endoscopic field of view. Three slender instruments are integrated into a single 8-mm-OD trocar, supported by a compact actuation unit for high-precision control. We further developed an optimization-based inverse kinematics model for the redundant robotic instrument, achieving a 0.9-mm root mean square error (RMSE) in open-loop path-following tasks. To address the challenges of resecting hard osseous tissues with miniaturized instruments, we integrated a thulium laser fiber to deliver energy to the confined spinal anatomy; this laser also serves to cauterize soft tissues, such as the venous plexus, for effective hemostasis with saline circulation. The MicroSpine system is designed to achieve direct, complete, and minimally invasive anterior lumbar nerve decompression via a single 3-cm incision. The system's performance was systematically validated, beginning with reachability assessments to bilateral articular processes using a three-dimensional (3D)–printed, patient-specific vertebral phantom model, followed by in vivo animal experiments and human cadaver tests. Our findings indicate that this robot-assisted protocol enables efficient decompression, typically completed within 15 min with an estimated intraoperative blood loss of only 5 ml. Consequently, the MicroSpine system expands surgical indications for OLIF, including disc herniation, articular process hypertrophy, and ligament hypertrophy.

RESULTS

Robotic system design

The robotic system primarily consists of a bedside robot (Fig. 1A) and a surgeon control console (Fig. 1B). To minimize radiation exposure, the control console can be strategically positioned either adjacent to the operating table or in a separate room. A custom cart-mounted rigid robotic arm (xMateER7 RPO, ROKAE, Shenzhen, China) accurately positions the trocar at the patient's surgical site. Surgeons control the system via two joysticks, receiving real-time visual feedback from both a steerable endoscopic camera and a fixed trocar-mounted camera. Laser energy for resecting degenerative spinal structures and achieving intraoperative hemostasis is delivered via an optical fiber connected to a thulium laser generator (SRM-T2F, Raykeen, Shanghai, China).

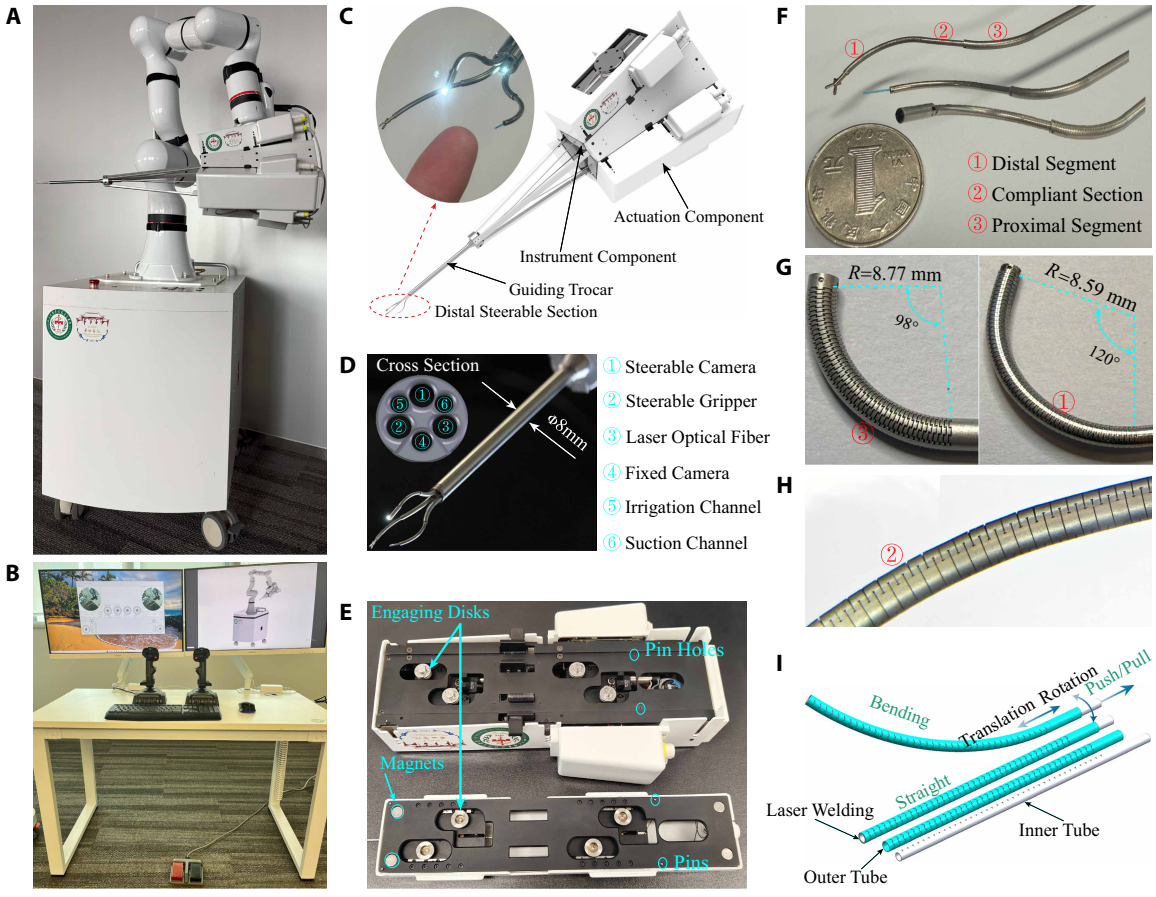

Fig. 1. Robotic system designed for minimally invasive anterior lumbar nerve decompression. (**A**) Bedside robot. The robotized instruments and actuation unit are mounted on a rigid robotic arm. (**B**) Surgeon control console. Surgeons manipulate two joysticks to control instruments, with endoscopic views displayed on screens. (**C**) Actuation unit for the instruments and the guiding trocar, supporting rapid instrument component release and assembly. (**D**) Steerable sections of instruments and the guiding trocar, featuring six specialized channels for instruments and saline circulation. (**E**) Detached instrument components and actuation components. (**F**) Steerable segments of the dual-segment architecture. (**G**) Tenon-mortise slits of the steerable segment. (**H**) Passive compliant section featuring "I"-shaped slits. (**I**) Schematic representation of the CPPR-based steerable segment. Each segment is formed by two concentric hollow steel tubes, facilitating the integration of a secondary segment or tip tool; this dual-segment design provides enhanced dexterity and an expanded operational workspace.

Both the instruments and their respective actuation units are mounted onto the rigid robotic arm (Fig. 1C). Each instrument is designed as a modular assembly consisting of an actuation component and an interchangeable instrument component, a configuration that facilitates rapid assembly and disassembly (movie S1). The three actuators are conically arranged to integrate tip-mounted tools. Figure 1D shows the instruments' distal section and the guiding trocar. The trocar integrates six channels: three for steerable instruments (steerable endoscopic camera, gripper, and laser fiber), two for saline irrigation/suction, and one for a fixed endoscopic camera. The steerable camera provides surgical site visualization, and the fixed camera monitors instrument shape. A saline-filled environment is essential for cleaning and cooling the surgical field, so the irrigation and suction channels create a saline circulation loop. The trocar was miniaturized to an OD of 8 mm and an ID of 7.6 mm, facilitating a small percutaneous incision to access the vertebral bodies. The steerable sections of the instruments are able to retract fully within the trocar or extend as required for surgical manipulation. Each instrument comprises a dual-segment CPPR arm (fig. S9) with an integrated tip tool: an endoscopic camera (OVM6946, Omnivision, USA), a gripper (GM-FB-C-N-10-1200, Grit, China), or a thulium laser fiber (Raykeen-365-300, Raykeen, China). The 0.9-mm hollow lumen of each CPPR instrument provides sufficient space to accommodate the camera signal wire (0.6 mm), the gripper actuation wire (0.5 mm), and the laser fiber (0.365 mm).

Pins and magnets are integrated at the interface between the instrument component and actuation component (Fig. 1E) to ensure precise alignment of transmission disks. All electric motors (ECU16036H12-S108, MOONS', China) are housed in the actuation component, with engaging disks transmitting motion to the instrument component (fig. S11B). The structure of the robotized steerable instruments was inspired by a CPPR arm architecture. As illustrated in Fig. 1F, the distal segment passes through the hollow lumen of the proximal segment via the thin-walled CPPR structure. A passive compliant segment featuring "I"-shaped slits is integrated into the distal segment, facilitating smooth sliding within the proximal segment. The specific configurations of the steerable and compliant segments are detailed in Fig. 1 (G and H), and the geometric parameters of the tubes are listed in table S1. A single steerable segment consists of two concentric hollow steel

tubes featuring symmetrically aligned patterned slits, which are fixed at the distal tip through laser welding (Fig. 1I). The relative axial pushing or pulling of the inner tube deforms the steerable segment, thereby enabling 2D arc bending. By integrating rotational and translational DoFs (Fig. 1I), each segment achieves 3 DoFs (bending, rotation, and translation). This configuration allows all instruments to be controlled either individually or in coordination to achieve precise tip positioning. Figure S11 (A and B) illustrates the core actuation mechanism of a single segment, with a spline-thread shaft connected to the inner tube. Rotation of two gears enables segment bending or rotation. Furthermore, the instrument components are secured to the actuation unit via specialized locks and grooves, and quick-release buttons enable the rapid replacement of instruments (movie S1).

Single-arm performance evaluation

The maximum bending angles of the proximal and distal segments reach 98° and 120°, respectively (Fig. 1G). With a maximum relative translation distance of 10 mm, the tip tool can achieve various poses (Fig. 2A). The end effector of one dual-segment arm provides a workspace of ~72.66 cm^3 (Fig. 2B), even when the translation DoF of the proximal segment is deactivated. A 120° field-of-view endoscopic camera at the tip provides surgeons with an expansive surgical view.

Motion accuracy is paramount for surgical safety and is intrinsically linked to both mechanical precision and the efficacy of the kinematic model. We developed an optimization-based inverse kinematics model to calculate actuation inputs for target tip positions. To evaluate

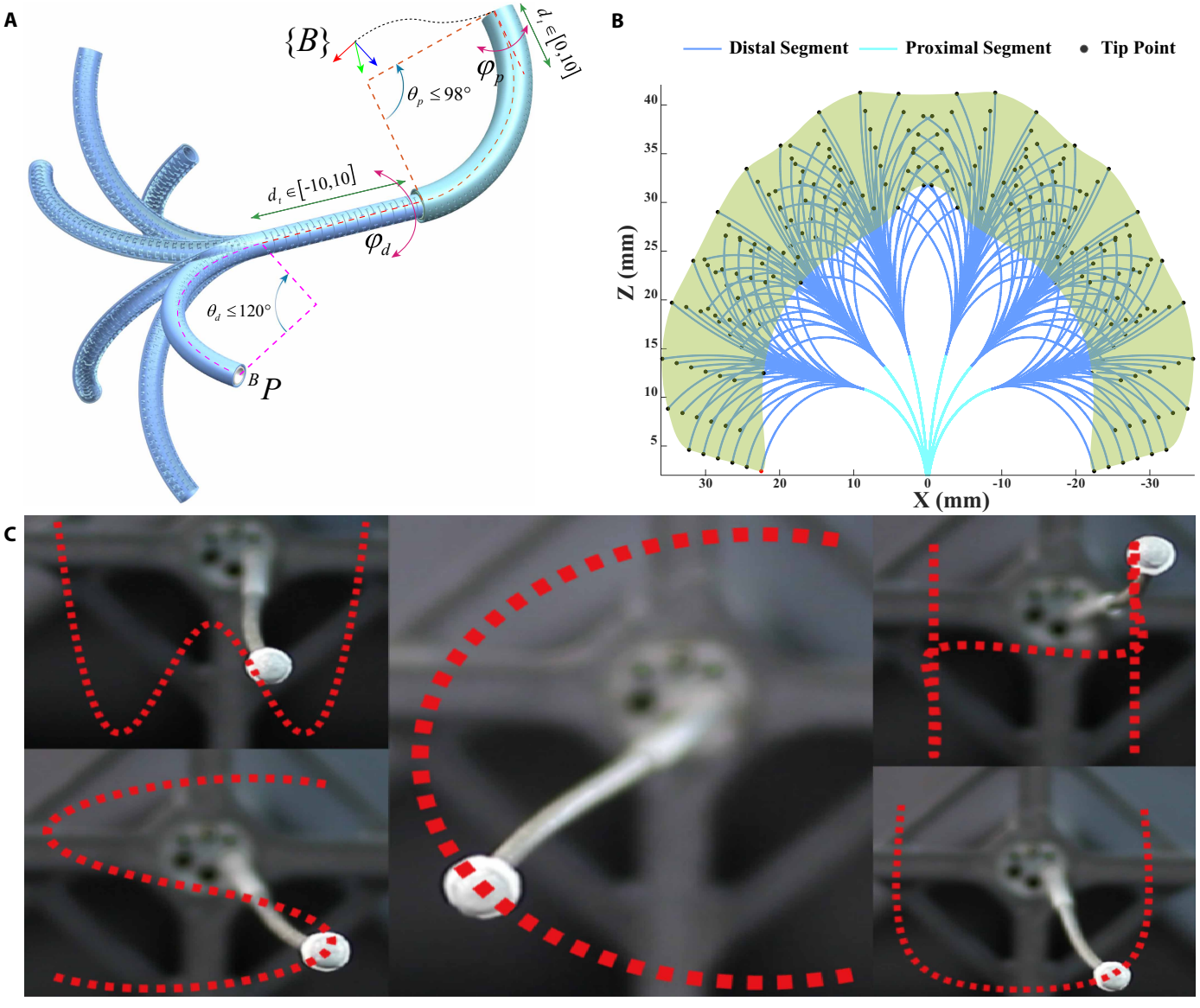

Fig. 2. Tests on the robot's basic performance, including coverage of workspace and following given paths. (**A**) Parameterized robot arm shape. The distal segment passes through the hollow lumen of the proximal segment, enabling high dexterity with large bending angles. (**B**) Cross section of the end-effector workspace with the translation DoF of the proximal segment deactivated. (**C**) Open-loop 2D path-following.

its performance, the robotic arm followed a series of 2D paths, designated as "WCHSCU," each of which consisted of 360 discrete points. As shown in Fig. 2C and movie S2, both segments bent and translated simultaneously, guiding the tip position marker along the path points. Repeatability was further validated using identical "C" paths, and a spiral path was used for 3D path-following evaluation. Position errors between the desired and actual paths are shown in fig. S2, with a maximum error of 1.65 mm and a RMSE of 0.9 mm under open-loop control. The maximum error occurred at the "W" path because of sharp turning points. When following the smooth "C" path, the RMSE and maximum error were reduced to 0.85 and 1.1 mm, respectively. Throughout these experiments, the velocity of the marker was consistently maintained at ~9 mm/s. The error sources include mechanical assembly imperfections, measurement inaccuracy from the optical sensing system (OP-M620, AIMOOE, China), and inertial effect at sharp turning path points. In addition, the axial elasticity of the passive compliant section (exhibits spring-like behavior) results in an actual push/pull displacement at the steerable section that is smaller than the commanded configuration, thereby introducing kinematic inaccuracies. Reducing velocity to around 4 mm/s improved path "W" performance, yielding an RMSE of 0.88 mm and a maximum error of 1.3 mm. Although limited lumen space precludes the integration of tip-mounted internal sensors for closed-loop control, the current open-loop path-following accuracy is deemed feasible for resecting degenerative spinal structures, given that surgeons can effectively use real-time endoscopic visual feedback for instrument guidance.

Stiffness is a critical performance metric directly affecting surgical maneuverability. Therefore, we systematically evaluated the stiffness of both robotic segments. The steerable segment was connected to a force sensor (SBT641, SIMBATUOCH, China) via a steel wire. As shown in Fig. 3A, the outer tube was secured in a fixed position, and a linear stage applied displacement to the inner tube to generate relative push/pull distance. The distal segment's passive compliant segment was clamped to eliminate compliance effects. The inner tube push distance served as the independent variable, with the corresponding tip force recorded as the experimental output. Figure 3B presents the measured force across a push distance ranging from 0 to 4 mm, with an increment of 0.1 mm. As a result, the maximum tip forces generated by the proximal and distal segments were 4.4 and 2.6 N, respectively, sufficient for manipulating most elastic biological tissues. In addition, a 100-g weight was hung at the tips of the two segments to evaluate their payload-carrying capability. Key snapshots of this process are shown in Fig. 3 (C and D), with the full motion documented in movie S2. Both segments successfully lifted the weight, with the distal segment achieving a 5-mm maximum push distance because of its slender body and lower structural stiffness. Although the material is stainless steel and each segment has a wall thickness of 0.1 mm, the stiffness increased notably with the increase of bending angle. This phenomenon results from the tenon-mortise slit design, where larger bending angles facilitate mechanical interlocking between the tenons and mortises. Peak stiffness is achieved once all tenon-mortise slits are fully interlocked.

Beyond testing the stiffness of the two segments individually, we also evaluated the stiffness of the dual-segment robotic arm (fig. S3A). The distal segment tip interacted with the force sensor, with a 3-mm push distance applied to the proximal segment. The translational DoF of the distal segment was varied across four settings [translation distance (d_t) = −6, −3, 3, or 6 mm], and the resulting tip force was measured for each configuration. Predictably, extending the passive compliant segment from the proximal segment (d_t = 3 or 6 mm) reduces the recorded tip force, whereas retracting it (d_t = −3 or − 6 mm) leads to a measurable increase in force. The physical interaction between the robotic arm and the force sensor is illustrated in fig. S3B, with a comparative analysis of the forces under these four configurations presented in fig. S3C. At the settings of d_t = 3 mm and d_t = 6 mm, the interaction force exhibited a slight increase relative to the push distance, accompanied by visible deformation of the compliant segment (highlighted by dashed elliptical circles in fig. S3B, iii and iv), yielding a maximum tip force of ~0.2 N. Conversely, when the passive compliant section was retracted into the proximal segment, the interaction force rose notably as the push distance varied from 2 to 4 mm. Specifically, in the configuration where d_t = −6 mm and the push distance was 4 mm, the interaction force reached 0.658 N, with both segments maintaining an arch shape (fig. S3B, i and ii). This confirms that tip manipulation force can be regulated by adjusting d_t. Such a mechanism allows for high-stiffness configurations suitable for manipulating elastic intervertebral disc, and low-stiffness configurations can be selected for nerve dissection. Furthermore, the proximal segment's translational DoF ensures the maintenance of an expansive workspace even when the distal segment is in a retracted state.

To quantify payload resistance, we attached a position marker to the arm tip and measured tip deviation between load-free and loaded conditions. As shown in fig. S3D, a single proximal segment was initially evaluated. We sequentially set the push distance acting on the inner tube to 1, 2, or 3 mm, and loads of 20 or 50 g were hung at the tip. Under the identical actuation settings, a smaller deviation of the tip position between load-free and with-load scenarios indicates a higher structural stiffness. The recorded deviations are detailed in table S4. For the single proximal segment, the tip deviation decreased as the push distance increased, demonstrating that the tenon-mortise slits gradually interlocked to enhance structural rigidity. The deviation was only 2.12 mm, whereas the load was 50 g, and the push distance was 3 mm, showing the high stiffness of the proximal segment. Similar tests were conducted on the dual-segment robotic arm with the distal segment fully extended from the proximal segment. Because of the extended cantilever length and the inherent flexibility of the distal segment (dominated by the passive compliant section), the tip marker exhibited downward deflection (fig. S3D). The tip deviations for various distal segment actuation configurations are listed in table S4. Although the load was 50 g and the bending angle in load-free condition reached around 70°, the maximum deviation was 16.8 mm. Correspondingly, an increase in push distance moved the weight upward. In summary, because the single proximal segment provides the high stiffness necessary to withstand external forces, the dual-segment configuration exhibits controlled compliance under external payloads.

In addition, a conventional square-slit CPPR arm was developed to compare the ability of withstanding load with the tenon-mortise design, maintaining identical cross-sectional cut area, slit width, slit count, and gap distance. A 50-g load was also applied at the tip, and the inner tube was actuated with push distances of 1, 2, and 3 mm. Initially, the load was exerted in the bending plane (radial load, as illustrated in fig. S10A). At a 1-mm push distance, the square-slit design exhibited limited ability to withstand the load, and the increase of push distance failed to mitigate the shape deformation. In contrast, the tenon-mortise design demonstrated superior structural stability under load (fig. S4A). Subsequent tests involved applying a lateral

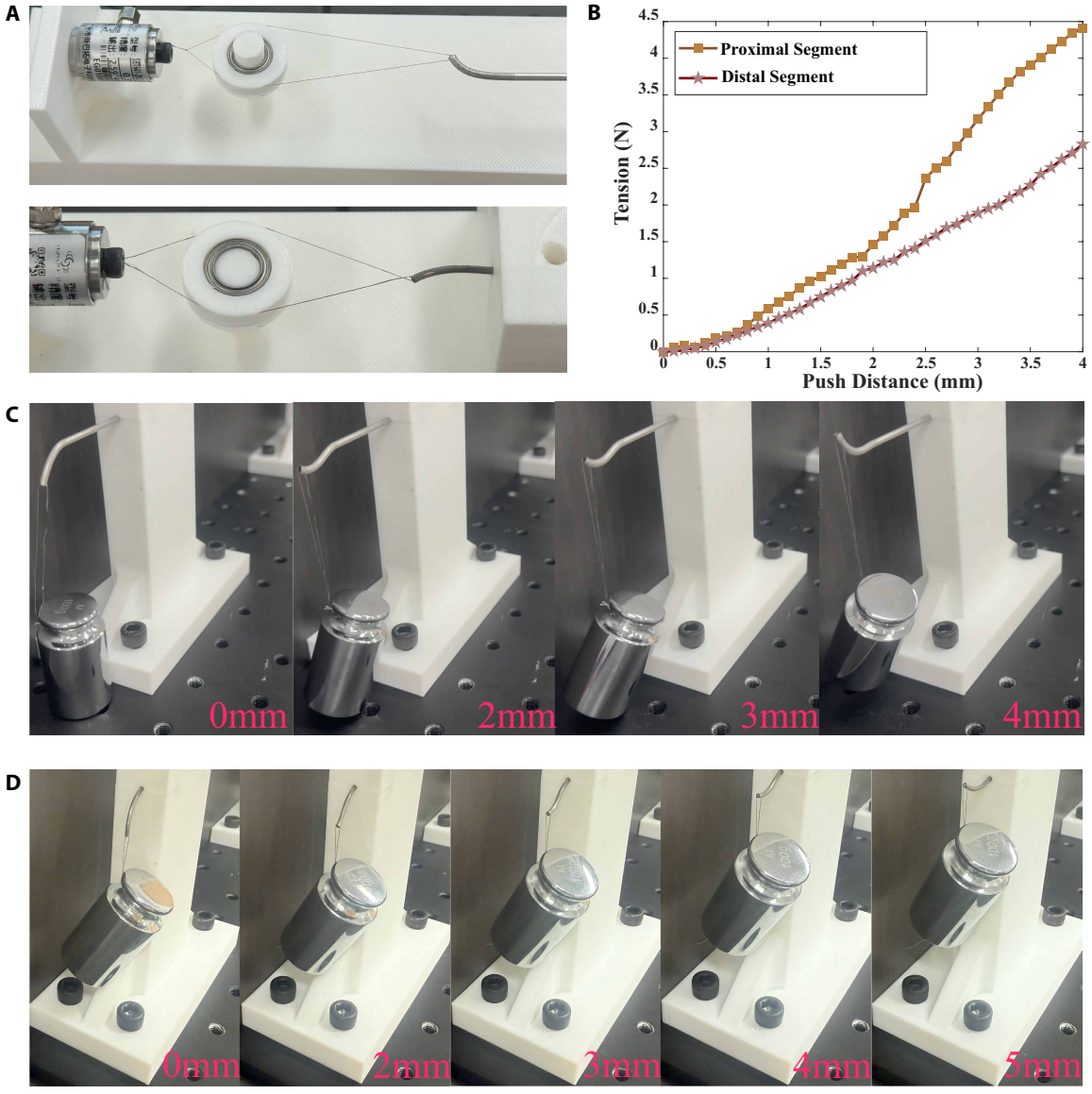

Fig. 3. Single-segment stiffness testing. (**A**) Tension testing setup. The tip of steerable section connects with a force gauge using a wire and a pulley. (**B**) Tension with various push distances acted on the inner tube. (**C** and **D**) The proximal (C) or distal (D) segment is dragging a 100-g weight, and the distance value at the bottom right of each snapshot is the push distance applied on the inner tube.

load to the side of the arm (fig. S10A). As a result, the square-slit design proved inadequate in withstanding lateral forces (fig. S4B). Bending snapshots presented in fig. S4C confirm that no interlocking occurs in the square-slit design, thereby validating the mechanical advantages of the tenon-mortise architecture. Given that the internal slits of the inner tube remain invisible during physical testing, finite element method (FEM) analysis was used to investigate the deformed shape of the tenon-mortise design and verify simultaneous interlocking across both tubes. The analysis result, shown in fig. S4D, indicates that the redundant interlocking mechanism enhanced both torsional rigidity and flexural stiffness, because the second moment of inertia of the tube increased upon interlocking. Conversely, a lot of vacant space in the square-slit design results in a relatively lower second moment of inertia, compromising its overall stiffness.

Robot arm coordination

The maneuverability of the robotized instruments was assessed, focusing on the visual field and multiarm coordination. As shown in fig. S5A, the instruments performed tasks inside a narrow constrained workspace where four small rubber rings were arranged for manipulation. The entire robotic system was required to complete three sequential objectives: The gripper arm picked up the green rubber ring and placed it in a semiclosed corner (highlighted by the green arrow in fig. S5A); the gripper arm subsequently picked up the red, black, and blue rubber rings to hang them in the laser optical fiber arm; the gripper arm retrieved the three rubber rings and placed them onto three protruding columns in sequence.

During the execution phase, the operator first positioned the trocar using the rigid robotic arm and subsequently activated only the

slender instruments for task performance. Figure S5 shows key motion snapshots of instrument's motion. Throughout the procedure, the operator relied exclusively on real-time visual feedback provided by the two endoscopic cameras. To maintain a comprehensive view of the core manipulation area, the operator maneuvered the gripper arm and simultaneously controlled the steerable camera (movie S3). The steerable camera arm was initially extended from the trocar channel to capture a comprehensive view of the entire task space (fig. S5B). Then, the laser arm and the gripper arm reached the task space (fig. S5C), with the laser arm moving aside to clear the operational field for the gripper. As shown in fig. S5 (D and E), the gripper arm successfully retrieved the green rubber ring and placed it in a semiclosed corner measuring only 3 mm by 3 mm by 3 mm. Next, the operator coordinated the two instruments to collect the remaining three rings and hung them on the laser optical fiber arm, a process that required interarm coordination (fig. S5, F and G). During this step, the pose of the steerable camera was continuously adjusted to ensure that the manipulation area remained visible. Last, the gripper arm retrieved the three rubber rings from the laser arm (fig. S5H) and transferred them to the three protruding columns (fig. S5I). The entire coordination sequence was completed within ~3 min, as documented in movie S3. It is anticipated that task efficiency can be further enhanced by upgrading the surgeon-robot interface.

Surgical protocol of robot-assisted anterior decompression

The distinctive advantage of the MicroSpine resides in the slenderness, dexterity, structural stiffness, and effective multiarm coordination of its robotic instruments. Leveraging these integrated features, we propose a robot-assisted minimally invasive anterior decompression protocol, which follows standard OLIF steps, with the key difference in the decompression procedure.

The surgeon makes a small oblique abdominal incision while the patient's body is in the right lateral decubitus position (Fig. 4A). A retractor is subsequently advanced through this percutaneous port to the anterior side of the spine, during which the surgeon delicately moves aside the ureters and aorta to minimize the risk of iatrogenic trauma. To establish a stable surgical corridor (Fig. 4B), a screw is secured to the vertebra via the retractor, which is then fixed to the operating bed. Once the surgical corridor is established, the herniated disc is visualized, and an access port is created in the intervertebral disc to accommodate the robotic instruments. The rigid robotic arm advances the trocar through the corridor, and the laser arm resects the intervertebral disc under dual-endoscopic guidance (Fig. 4C). In the resection process, the saline irrigation and suction pumps work simultaneously to maintain a saline-filled circulation environment, which serves to evacuate surgical effluent and ensure the continuous clarity of the endoscopic cameras. The instruments are then advanced toward the posterior area of the spine to resect right-sided articular process osteophytes using the thulium laser. Throughout this process, surrounding nerves are meticulously dissected and protected by the gripper to prevent unintentional trauma (Fig. 4E).

The instruments are subsequently navigated to the left posterior area, which is typically inaccessible via standard OLIF. The thulium laser addresses central stenosis during the transition (Fig. 4F). Decompression is completed by resecting the left articular process osteophytes. The steerable camera is strategically positioned to maintain comprehensive visualization of the surgical site and preserves the necessary operational space for the manipulation instruments. The gripper is used to retract nerve roots, preventing iatrogenic injury (Fig. 4G) and to remove the resected osteophytes (Fig. 4H). Last, instruments are withdrawn, and the surgeon manually performs interbody fusion cage implantation to restore spinal stability (Fig. 4I).

In summary, standard OLIF procedures typically accommodate only one or two surgical tools in the constricted intervertebral disc space. In contrast, the slender and highly dexterous instruments facilitate the simultaneous resection of degenerative tissues in both the anterior and posterior spinal regions, including the complex anatomical structures of the bilateral articular process joints. The noncontact thulium laser beam provides precise tissue resection, and the laser arm itself can be used to retract soft tissues and nerves. Furthermore, the standard vertebral retractor used in this protocol provides sufficient fixation and dilation of the surgical site, thereby eliminating the necessity for additional specialized fixators for the MicroSpine system.

In vitro test on a 3D-printed human vertebral phantom model

The accessibility of key surgical sites and the coordination of the three instruments in the constricted vertebral space were first evaluated using a 3D-printed human vertebral phantom model. This physical phantom model was reconstructed from computed tomography (CT) scanning data of a patient, focusing on the L3-L5 lumbar vertebrae. As shown in Fig. 5A, the superior articular process, herniated parts of the intervertebral disc, and the central sequestrated intervertebral disc are labeled in red, black, and blue, respectively. The laser arm was used to sequentially approach these targets under real-time

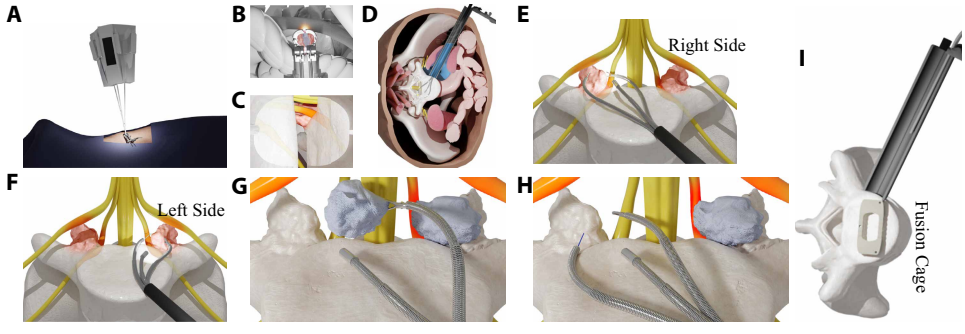

Fig. 4. Robot-assisted surgical protocol for anterior minimally invasive decompression. (**A**) The trocar is advanced through the anatomical corridor connecting the incision port to the vertebral body. (**B**) Initial limited visualization of the vertebra after the establishment of the surgical corridor. (**C**) Resection of the intervertebral disc by the thulium laser fiber, exposing the posterior spinal area. (**D**) Saline irrigation of the surgical site to facilitate laser resection and maintain endoscopic camera clarity. (**E**) Simultaneous deployment of the three robotic instruments at the right posterior spinal region for osteophyte resection. (**F**) Precise instrumentation control enabling access to the left posterior area, allowing for the treatment of central posterior stenosis. (**G**) Nerve root retraction using the gripper to mitigate the risk of iatrogenic injury during decompression. (**H**) Successful retrieval of resected degenerative tissue by the gripper. (**I**) Manual implantation of the fusion cage to restore spinal stability after the decompression procedure.

visualization provided by the steerable endoscope, and green laser light was used to simulate resection and validate reachability. Subsequently, the rigid arm advanced the trocar along the axial direction. As the trocar reached the anterior aspect of the disc space, the slender instruments entered the intervertebral space, providing a rigorous test of their dexterity and performance under conditions simulating severe intervertebral disc stenosis. As the trocar reached the anterior side of the intervertebral disc space between L4 and L5, the slender instruments entered the intervertebral disc space, fully testing the instruments' dexterity and simulating conditions associated with intervertebral disc stenosis. Visibility, accessibility, and maneuverability were validated across six critical surgical zones: the left superior and inferior articular processes, the posterior midline of the L5 and L4 vertebrae, and the right superior and inferior articular processes. The initial target was the left superior articular process, a region notably challenging to access during standard OLIF (Fig. 5B). All three instruments successfully navigated the left herniated intervertebral disc, confirming the laser arm's capacity to establish a path to the posterior region via the dexterous robotic architecture. The endoscope maintained a view of the target site (Fig. 5C), and the gripper's distal segment successfully rotated toward the left inferior articular process, demonstrating notable dexterity for posterior access.

The instruments were subsequently controlled to reach the right side of the posterior area for further accessibility testing. The robotic instruments successfully crossed the spinal canal at the L5 posterior midline to reach the right superior articular process (Fig. 5C). The orientation of motion was confirmed by the green light emitted from the laser optical fiber (Fig. 5D). By delicately adjusting the poses of the two manipulation instruments (the laser optical fiber and gripper), both the laser fiber and the gripper successfully reached the right superior and inferior articular processes (Fig. 5E) under continuous endoscopic visualization (Fig. 5F). The result also indicated that the instruments passed the midline of vertebra L4. Similarly, the distal segments of the two manipulation arms were adjusted to bend beside the right inferior articular process, allowing the instruments to successfully reach all the six target areas.

Across 20 repeated trials, the success rates for reachability were 100% for the left posterior region and 95% for the right posterior region. The single failure occurred during the initial trial when the laser arm was incorrectly operated because of inaccurate anatomy recognition; all subsequent trials were performed successfully. Navigating the tortuous articular processes on the left side required the robotic segments to achieve relatively large bending angles. Specifically, the proximal and distal segments of the gripper arm reached angles of ~50° and 70°, respectively, both of which remained within their maximum operational limits (Fig. 5B). For observing the instruments' shape, the OLIF retractor was not used in this experiment, meaning that the intervertebral disc space remained unexpanded. Given that the patient-derived CT data showed an intervertebral distance of only ~6 mm, the proximal segments of the three instruments operated in extremely close proximity to one another. In clinical practice, surgeons typically use retractors to dilate this space, especially when addressing spinal stenosis. These results collectively validate the system's robust capability to navigate confined and complex spinal anatomy.

In vivo animal experiment

Given the paucity of clinical experience regarding the use of lasers for lumbar nerve decompression, the precise calibration of the thulium laser generator's operational parameters is imperative. These settings must be meticulously adapted to enable various surgical maneuvers, including the resection of elastic fibrous rings, nucleus pulposus, and dense osseous structures, as well as the cauterization of venous vessels for intraoperative hemostasis. To rigorously evaluate the overall performance of the robotic system, we conducted validation using a porcine spine, focusing specifically on the surgical efficacy of the robotic instruments.

The pig was anesthetized and secured on the operating bed in a position aligned with standard OLIF procedures (Fig. 6A and fig. S6). The surgeon established a surgical corridor to the anterior side of the lumbar vertebrae using a small oblique abdominal incision and a lateral retractor (OLIF25, Medtronic, USA). Under comprehensive endoscopic guidance, the surgeon manipulated the robotic trocar via joysticks (movie S4). To optimize visualization and facilitate hemostasis, we irrigated saline into the L4-L5 disc space, with simultaneous suction deployed for the continuous removal of debris. Upon instrument extension, the steerable camera was adjusted to visualize the targeted resection area (Fig. 6B). To identify the optimal laser configurations, including power and pulse energy, we initially used a setting of 2 J (pulse energy) and 20 W (power). However, these parameters proved insufficient for the resection of tough fibrous tissue, necessitating an adjustment to 4 J and 40 W. With these refined settings, the laser effectively resected the fibrous ring, with tissue fragments observed floating in the saline environment (Fig. 6Bi and movie S4). During the procedure, transient bleeding was observed (Fig. 6Cii), which momentarily

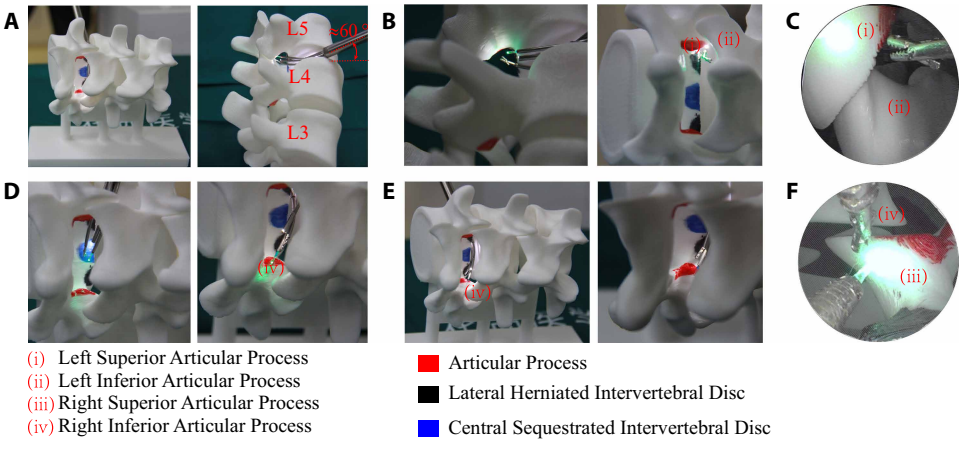

Fig. 5. Accessibility validation in a 3D-printed human vertebral phantom model. (**A**) Experimental setup and side view illustrating the positional relationship between the vertebrae and the robotic trocar. (**B**) Simultaneous deployment of the three robotic instruments at the left articular processes to simulate osteophyte resection. (**C**) Endoscopic visualization of superior and inferior articular processes on the left side. (**D**) Precise instrumentation control as the system approaches the right posterior region. (**E**) Side view and close-up detail of instruments positioned at the right superior articular process. (**F**) Endoscopic view of manipulating the right superior and inferior articular processes.

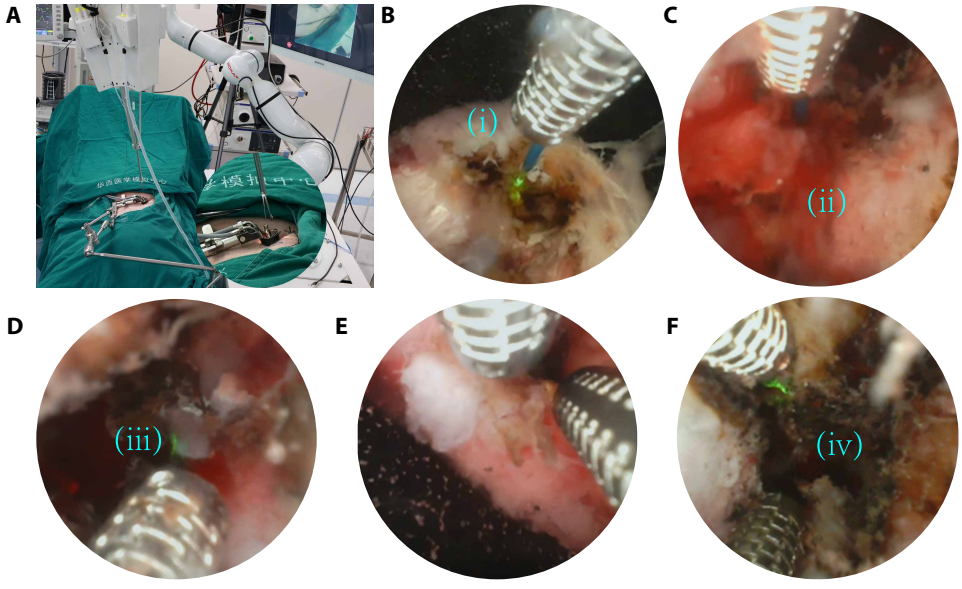

Fig. 6. Evaluation of the robotic system in an in vivo porcine spinal structure, focusing on surgical tool functionality and accessibility to a series of targets. (**A**) The anesthetized pig is in the lateral decubitus position; the rigid robotic arm aligns the trocar with the standard OLIF retractor. (**B**) Initiating an opening of the fibrous ring. (**C**) Management of intraoperative bleeding via irrigation and suction to restore visual field clarity. (**D**) Resection of the nucleus pulposus to establish access to the posterior spinal area. (**E**) Coordinated manipulation of tissues using two robotic instruments. (**F**) Laser-assisted resection of the right posterior superior articular process.

compromised visual clarity. In standard OLIF, surgeons typically use electrocoagulation to manage bleeding. Our system leverages the thulium laser for venous cauterization by using differentiated parameter settings. The finalized hemostasis configuration (2 J and 20 W) effectively cauterized the veins without causing thermal damage to adjacent nerves or fibrous tissues. Integrated saline circulation successfully evacuated the turbid fluid, restoring surgical site visibility. Because the hemorrhage was managed immediately without requiring instrument exchange, the bleeding episode lasted only ~10 s, with an estimated total intraoperative blood loss of merely 5 ml.

After hemostasis, the laser continued to resect the intervertebral disc to establish a passage to the posterior area. Figure 6D shows endoscopic visualization of nucleus pulposus resection, which is characterized by a softer consistency than the fibrous ring. The total duration for full intervertebral disc resection was ~90 s, notably shorter than the 5 min typically required in standard OLIF because of the avoidance of frequent instrument exchange and endoscope cleaning. The thulium laser enables simultaneous resection and hemostasis, with saline circulation removing resected tissue. In this step, coordinated multiarm manipulation enhanced overall efficiency. The gripper arm was used to retract resected tissue, thereby clearing the laser's operational path (Fig. 6E). Once the anterior-posterior passage was established, the instruments were paused for 20 s to fully clear the surgical field before advancing to the posterior area. Laser parameters were subsequently adjusted to 4 J and 60 W for the resection of the articular processes. The laser successfully resected the right superior and inferior articular processes within ~2 min (Fig. 6F), and the gripper arm provided assistance by retracting floating tissues.

This in vivo animal experiment validates the thulium laser as a versatile and precise tool for both lumbar decompression and hemostasis. Because the basic structure of the porcine spine differs from that of the human spine [the height of intervertebral disc in lumbar is only around 3 mm (*51*)], there is almost no space to enter the left side of the posterior area. In this experiment, the effectiveness of resecting intervertebral disc, hemostasis, and multiarm coordination was evaluated. Because of the narrow space of porcine spine, we did not mount the gripper at the tip of one robot arm, which only worked as a stripper. By tuning the parameters of the laser beam, we found that although the system provides precision in resecting tissues, it only covers a small area of tissue. Therefore, the distal dexterity of robotic instruments is necessary to bring the laser to a series of the desired targets. The successful validation on the porcine spine also demonstrates the notable accessibility of the slender and dexterous robotic instruments.

Human cadaver tests

To further evaluate the clinical feasibility and anatomical adaptability of the MicroSpine system in a human context, we conducted human cadaver tests (Fig. 7). The specimen was secured in the right lateral decubitus position on the operating bed. Following the standard OLIF clinical pathway, the surgeon made a skin incision of ~3 cm in length, stripping the muscle until the intervertebral disc (between vertebrae L3 and L4) was fully exposed (Fig. 7A and fig. S7). A guidewire was inserted into the disc, and cone-beam computed tomography (CBCT) (OEC 3D Supreme, GE Healthcare, USA) confirmed surgical targets (fig. S8A).

Next, the lateral retractor was placed and fixed on the operating bed, dilating a disc space of ~8 mm between the two vertebrae for the three robotic instruments. A 7 mm–by–16 mm access port was manually created at the disc (Fig. 7B). The depth of the incision on the intervertebral disc was only around 2 mm (fig. S8, B and C). The rigid robotic arm was then used to navigate the trocar through the retroperitoneal space, ensuring that it was aligned to the target disc (movie S5).

Upon the trocar reaching the anterior disc space, the three slender instruments were extended into the intervertebral corridor. Saline was irrigated into the surgical site to create a saline-filled environment. The steerable endoscope provided real-time visualization of the intervertebral disc space (Fig. 7C). The laser instrument (parameter settings: 4 J and 40 W) was first used to resect the intervertebral disc, creating a dedicated passage to the posterior region. After ~2 min, the intervertebral disc was fully resected, and the steerable camera passed through the passage to visualize the posterior area (Fig. 7D). Next, the three robotic instruments were navigated toward the posterior spinal canal to perform bilateral decompression.

The laser arm and gripper arm subsequently began to expose the superior and inferior articular processes (Fig. 7Ei). The laser parameters were adjusted to 4 J and 60 W for resecting the superior and inferior articular processes (Fig. 7Eii). To confirm that the instruments reached

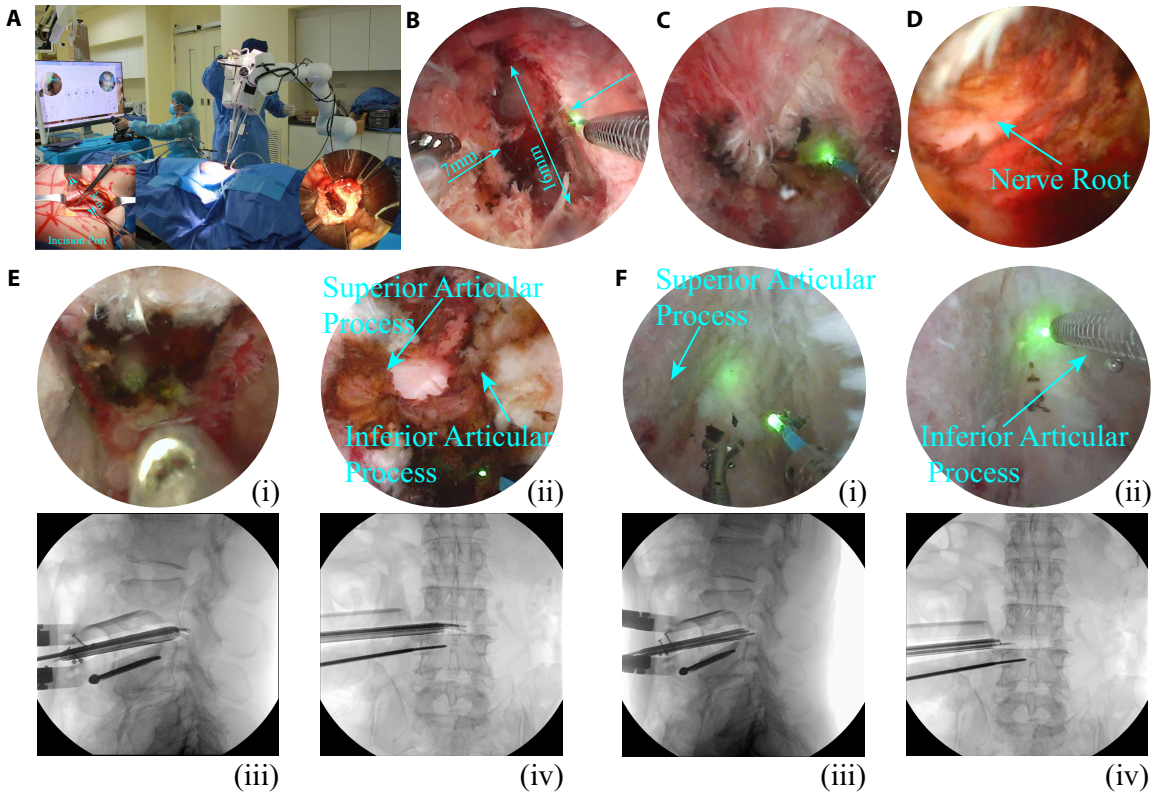

Fig. 7. Human cadaveric evaluation of the MicroSpine system. (**A**) Human cadaver positioned in the lateral decubitus position, with the robotic trocar aligned. (**B**) Surgeon incised a small port on the intervertebral disc to label the entrance for the instruments. (**C**) Endoscopic visualization of the robotic instruments as they enter the intervertebral disc space. (**D**) Steerable camera arm passed through the small passage on the intervertebral disc to collect the view of posterior area. (**E**) Decompression at the right side of the posterior area. (i) Resecting elastic tissue around the right side of superior and inferior process. (ii) The laser beam was resecting the hard spine tissues. (iii and iv) Lateral and frontal fluoroscopic images of the instruments on the right side. (**F**) Decompression at the left side. (i and ii) Endoscopic visualization of the laser arm resecting the superior and inferior articular processes. (iii and iv) Lateral and frontal fluoroscopic images of the robotic instruments at the left side.

the target surgical site, fluoroscopic images were used to localize the instruments in the spine (Fig. 7E, iii and iv). The laser arm was then directed to resect the two articular processes, completing the resection within just 80 s (movie S5).

The three instruments then navigated to the superior and inferior articular processes on the left side. Similarly, the two manipulation instruments reached the target area (Fig. 7F), and their positions in the spinal structure were also confirmed using fluoroscopic images (Fig. 7F, iii and iv) before resection. To resect the articular process (Fig. 7F, i and ii), the gripper arm stripped the tissues, and the laser beam precisely worked on the hard osseous structure. Last, the instruments withdrew from the retractor corridor, and the surgeon manually inserted a fusion cage into the intervertebral disc (fig. S7B).

The durations for the steps in the procedure were as follows: 3 min for resecting the intervertebral disc, 1 min for resecting the articular process on the right side, 3 min for moving to the left side, and 5 min for resecting the articular process on the left side. The entire decompression procedure, from resecting the intervertebral body to withdrawing the trocar from the retractor, took ~15 min. Much of this time was spent confirming the surgical target using the CBCT machine. It should be noted that the human cadaver was not diagnosed with degenerative spinal disease, and bleeding issues were not observed because the cadaver had been stored in a refrigerator for more than 1 year. The success of effectively reaching the tortuous posterior area and resection also demonstrates the clinical value. The instruments' dexterity and large workspace enable resection of degenerative tissues in both the intervertebral disc and posterior spinal areas.

DISCUSSION

In this study, motivated by the limitations of available instruments in standard OLIF surgery, we designed the robotic system MicroSpine to enhance the surgical outcome of lumbar nerve decompression. This technique leverages the natural anatomical corridor and minimal invasiveness of OLIF and overcomes its inherent shortcomings related to the inability to access posterior areas via an anterior route. The slender, dexterous robotic instruments enable direct and complete resection of anterior and posterior degenerative spinal structures, extending access to hypertrophic facet joints and ligamentum flavum, pathologies inaccessible in standard OLIF. Standard OLIF surgery is able to resect the pathological tissues at the anterior area and decompress the nerves by dilating a space, leaving the osteophyte at the posterior area unaddressed. Our system transforms OLIF from an indirect decompression technique into a direct decompression strategy, notably expanding its surgical indications. Patients suffering from both anterior and posterior lumbar canal stenosis would benefit from a complete, minimally invasive anterior approach, potentially

reducing iatrogenic trauma, intraoperative blood loss, and complications. This robot-assisted OLIF paradigm may represent a meaningful advancement in spinal surgery, particularly for the elderly or high-risk patients who are poor candidates for traditional posterior decompression. The duration of decompression procedure was reduced to 15 min compared with the 1 to 1.5 hours typically required for standard OLIF (*52*, *53*). In addition, the blood loss was also reduced compared with standard OLIF. As an estimation, only around 5 ml of intraoperative bleeding will occur in future clinics, because the saline pressure could also minimize bleeding and the thulium laser beam could immediately perform hemostasis. No iatrogenic trauma occurred during the study, which potentially shortens the postoperative hospitalization stay from 1 week (standard OLIF) to 1 day (using MicroSpine).

MicroSpine is inspired by classic multiarm surgical robots comprising a bedside robot and surgeon control console (*44*, *54*, *55*). The key features of MicroSpine lie in the robotized instruments and kinematics model. Each instrument has a slender body of 2 mm, 6-DoF dexterity (large bending angle), and maneuverability (withstand radial and lateral payloads). Multiarm coordination enables effective surgical manipulation. A compact actuation unit enables rotation, bending, and translation DoFs, with an 8-mm miniaturized trocar integrating six channels. A dual-camera system provides comprehensive surgical visualization. This system is specifically designed for lumbar nerve decompression, with potential applications to other orthopedic surgeries.

We combined the advantages of CPPR arms with high-precision laser cutting technology to develop the slender and dexterous robotic instruments. The width of tenon-mortise slits on the stainless steel tube is only 30 μm, and the tube wall thickness is 0.1 mm, resulting in a slender arm that leaves a hollow space for the tip tool. This design also allows for ease of actuation, because bending, rotation, and translation are integrated at the rear end. The hollow space of CPPR accommodates the endoscopic camera signal wire, actuation wire for the gripper's opening and closing, and thulium laser optical fiber.

Despite the robotic instrument's slender and hollow design, it maintains relatively high stiffness in the steerable section because of the tenon-mortise slits. When bending occurs, the tenon and mortise interlock to enhance rigidity. The "I"-shaped slits in the distal segment passively adapt to the shape of the proximal segment. Because the entire instrument has a translation DoF (Q_p in fig. S12), the distal tool can achieve various poses. This allows the system to adjust the length of extension from the proximal segment (Q_d in fig. S12) to regulate stiffness for nerve or osseous tissue manipulation.

The steerable segment's arched shape enables the piecewise constant curvature assumption for forward kinematics. A nonlinear forward kinematics model was used to develop an optimization-based inverse kinematics model, with a penalty function added to prioritize distal segment motion. Real-time instrument shape estimation enables future surgical navigation integration.

Although the stiffness of the CPPR-based instrument is suitable for handling soft tissues like retracting nerves, it is insufficient for resecting hard pathological degenerative structures. To address this, we integrated a thulium laser optical fiber into the instrument's hollow space to provide the energy necessary for resection. The laser's operation requires a liquid environment, so we incorporated saline irrigation and suction channels in the trocar to establish circulation, which cleans the endoscopic cameras and evacuates effluent. Adjustable laser energy enables both resection and hemostasis.

The evaluation of MicroSpine was systematically organized. One 3D-printed human vertebral phantom model whose CT scanning data was from a real patient diagnosed with spinal degenerative diseases was first used to test the reachability to a series of key surgical targets. Because there was no prior experience in decompressing lumbar nerves with thulium laser, an in vivo animal experiment was conducted to further investigate the system's performance, demonstrating its capability to resect intervertebral disc and articular processes in the posterior area. The thulium laser could also be used for hemostasis immediately, which needs no instrument interchange, and intraoperative blood loss could be reduced. Last, overall performance was evaluated on a human cadaver, consistent with operations on patients (excluding anesthesia), showing that MicroSpine provides a comprehensive view of the surgical site and enables dexterous surgical manipulation in the target areas.

The system also has some limitations. First, the kinematics model was built on the basis of piecewise constant curvature assumption (*56*, *57*), and the shape of the robotic arm does not necessarily follow an arch when faced with external disturbance, which leads to inaccuracy. No internal sensor was integrated in the steerable section because of the limited size of the central hollow lumen, so the control strategy is open loop. Accordingly, the surgeon could not obtain haptic feedback in surgical manipulation. Second, the human-machine interaction device is not intuitive for operation, which caused ineffectiveness. Third, the slenderness of the robotic arm also posed a challenge to integrating high-quality endoscopic cameras. Currently, the area of the endoscopic camera is 400 pixels by 400 pixels, and the focal length is only around 5 mm.

Our future work will focus on developing an intuitive surgeon-robot interface and integrating multimodal large language models to facilitate surgical scene understanding and intraoperative decision support. This will be achieved by fusing preoperative imaging, robotic kinematics, and real-time endoscopic video. For the sensing issue, we will investigate embedding a fiber Bragg grating sensor (*58*) at the robotic instruments to form a proprioceptive sensing mechanism. For the endoscopic camera image issues, an artificial intelligence model will be developed to enhance the quality and further reconstruct the 3D shape of the surgical site (*59*).

MATERIALS AND METHODS

Slender robot arm design

The dexterous slender robot arms were designed on the basis of CPPR architecture. Each robotic segment comprises two concentric, thin-walled stainless steel (304) tubes permanently fixed at their distal tips. Precision-machined tenon-mortise slits were cut into the steerable section, with the inner and outer tubes assembled at a 180° (fig. S9) phase shift to facilitate antagonistic movement. This configuration enabled controlled 2D arc bending through the relative axial translation (pushing or pulling) of the inner tube, which features an extended end for integration with the actuation unit (fig. S9). To ensure smooth mechanical transitions, a passive compliant section incorporating "I"-shaped slits was specifically designed for the distal segment, allowing it to adapt to the curvature of the proximal segment. All of the basic design parameters of the four tubes are listed in table S1. The patterned slits were fabricated using high-precision laser cutting technology (HLR-PD0520-200IPG, Han's Laser, China). The diameter of the laser beam is 30 μm and cutting power is 200 W, which means that

the slits' width is also 30 μm. For welding (two tubes' tip), we used laser welding technology (SF150, Han's Laser, China).

Apart from the basic parameters of each tube (OD, R_o; ID, R_i; and length of the steerable section, L; shown in fig. S10A), the geometric parameters of tenon-mortise slit parameters are optimized for simultaneous interlocking of inner and outer tube slits, thereby maximizing flexural rigidity and torsional stiffness during bending. As shown in fig. S10A, the tenon-mortise slits on one tube are determined by multiple parameters: central angle, β, representing the uncut area in cross section; length of tenon, l_s; gap distance, d_g, between adjacent slits; number of slits, N; number of tenon-mortise combination, n, in one slit; slit width, d_s; height of slit, d_h; and tilted angle, θ_s. Let $S_D = \{\beta, l_s, d_g, N, n, d_h, \theta_s\}$ denote the to-be-determined slit parameters for one single tube. S_D^o and S_D^i represent the parameters for the outer tube and the inner tube, respectively. In the following, the subscript and superscript "o" and "i" denote the parameter for the outer and the inner tube, respectively, and variables without subscript or superscript are applicable for both. The shape of the steerable section is assumed as an arch, and the dexterity for one segment can be mathematically expressed by the maximum bending curvature: $\kappa_m = \frac{\theta_m}{L}$, where θ_m is the maximum bending angle. When all of the tenon-mortise slits interlock together, the bending angle reaches the maximum value θ_m, and we require that the slits on the two tubes simultaneously reach the maximum value. As shown in fig. S10B, pushing or pulling the inner tube generates upward or downward bending. For the outer tube, the tenon-mortise slits extend while it bends upward, and the slits will compress when the segment bends downward. Therefore, we can obtain the relationship between the parameters and the maximum bending angle

$$\theta_m = \begin{cases} \theta_o^U = \dfrac{N_o d_s^o}{2 d_o \cos\theta_s^o} & \text{Upward} \\ \theta_o^D = \dfrac{N_o d_s^o}{2 d_o} & \text{Downward} \end{cases} \tag{1}$$

where θ_o^U and θ_o^D denote the bending angles calculated from the outer tube in upward bending and downward bending modes, respectively. Similarly, for the inner tube, parts of design parameters are also related to the maximum bending angle

$$\theta_m = \begin{cases} \theta_i^U = \dfrac{N_i d_s^i}{2 d_i} & \text{Upward} \\ \theta_i^D = \dfrac{N_i d_s^i}{2 d_i \cos\theta_s^i} & \text{Downward} \end{cases} \tag{2}$$

where θ_i^U and θ_i^U denote the bending angles calculated from the inner tube in the two modes, respectively. Hence, we can mathematically express the design goal that tenons and mortises on the two tubes simultaneously interlock together (the two tubes reach the maximum bending angle concurrently): $\theta_o^U = \theta_i^D, \theta_o^D = \theta_i^U$.

With the diameters and steerable section's length of the tubes, we build the objective function to find the optimal design parameters

$$\min. \left(\frac{1}{\kappa_m} \right) \tag{3}$$

This is to maximize the value of the maximum bending angle. The slit parameters are also mutually coupled. The number of slits and the slits' gap distance are related to the length of the steerable section: $N(d_s + d_g) = L$. For one slit, its length and the central angle β are related to the tube diameter: $\left(2l_s - \frac{2d_h}{\tan\theta_s}\right)n = (2\pi - \beta)R_o$. Another constraint is built to require the two tubes to reach the maximum bending angle simultaneously ($\theta_o^U = \theta_i^D$): $N_o \frac{d_s^o}{\cos\theta_s^o} = N_i d_s^i$. Each design parameter should also fall within a given range: $S_{Dmin} \leqslant S_D \leqslant S_{Dmax}$. Table S2 lists the boundary values of each design parameter. Then, the optimization problem is solved using Genetic Algorithm with mixed integers in MATLAB (algorithm settings: population size = 200, maximum iteration generation = 4000, and elite number = 60). The parameter central angle β directly rates to the stiffness, and we finalized its value through trial and error (manufactured tubes with different β values whereas other design parameters were kept same). The design parameters determining the "I"-shaped slits are illustrated in fig. S10C, consisting of central angle β_1, gap distance d_g^I, and gap height d_h^I. We set $d_g^I = d_g$ and $d_h^I = d_h$, and β_1 is the only variable to regulate the stiffness of the "I"-shaped section. Through multiple-trial manufacturing, we determined that $\beta_1 = 2.87$ is the optimal value for stiffness. Last, the design parameters of the tenon-mortise slits for the four tubes were finalized and are listed in table S3.

FEM analysis was conducted in Ansys Workbench, and the two tubes were meshed using the default element size. The two tubes were bonded at the tip. The rigid section of the outer tube exerted a fixed constraint, and a displacement of 2 mm was exerted to the inner tube to generate bending at the patterned section. The analysis is beneficial for initially validating the slits design method, and the results demonstrate that the slits of the two tubes interlock simultaneously. In a physical steerable arm, the slits of the inner tube (occluded by the outer tube) is invisible, so FEM is useful for design and initial evaluation.

Robot kinematics

A kinematics model maps between the tip pose of robot arm and the base frame. The shape of the robot arm was assumed to be an arch, and the geometric relationship between the bending angle and the push/pull distance was derived on the basis of work in (*60*), which is therefore abbreviated. We then built the forward kinematics model through a homogeneous transformation matrix. The shape of a single segment is assumed to be an arch (fig. S12), and the shape parameters of the whole arm include $S = \{Q_p, \phi_p, \theta_p, Q_d, \phi_d, \theta_d\}$, where Q denotes translation DoF, ϕ is rotation angle, and θ is bending angle (subscripts "p" and "d" denote the proximal and distal segments, respectively). Therefore, the tip pose P in the robot base frame $\{B\}$ can be solved by homogeneous transformation

$$\begin{aligned} {}^P_B T = {} & T_z(Q_p) R_z(\phi_p) T_x(R_p) R_y(\theta_p) T_x(-R_p) \\ & T_z(Q_d) R_z(\phi_d) T_x(R_d) R_y(\theta_d) T_x(-R_d) \end{aligned} \tag{4}$$

where $T_i(\cdot)$ and $R_i(\cdot)$ denote translation homogeneous transformation and rotation homogeneous transformation matrix about axis i, respectively. Then, P is mapped with shape parameter S: $P = f(S)$. In terms of the inverse kinematics, we aim to find the optimal shape parameter $\hat{S}$ to map with a given target tip point $\hat{P}$. We used constrained optimization approach to solve this hyper nonlinear problem, and this can be initially set as

$$\begin{aligned} & \hat{S} = \min \| f(S) - \tilde{P} \| \\ & \text{with respect to } S_{min} \leq S \leq S_{max} \end{aligned} \tag{5}$$

where $S_{min} \leq S \leq S_{max}$ constrains the boundaries of each DoF. To make the distal segment move with a larger distance in point-to-point movement, a penalty factor can be added at the loss function

$$\hat{S}_k = \min\left[\|f(S) - \tilde{P}_k\| - \left(\theta_k^d - \theta_{k-1}^d - \theta_k^p + \theta_{k-1}^p\right)\right] \quad (6)$$

The constrained problem has six variables, and we used Genetic Algorithm to obtain the optimal design parameters. In this optimization problem, we made the following settings for Genetic Algorithm: Population size is 50, the maximum iteration generation is 200, the elite count is 20, and the acceptable tolerance is 10^{-8}. To avoid jerky motion, the robot system first computes the actuation configurations for the starting point and the end point, respectively, and then cubic interpolation method is used to smoothen the variation of each motor. In addition, we used the proportion integration differentiation (PID) method to regulate the velocity.

3D-printed vertebral phantom model preparation

We obtained the fluoroscopic data [Digital Imaging and Communications in Medicine (DICOM) format] for a patient from West China Hospital, Sichuan University, and reconstructed the 3D spinal geometry using 3D Slicer software. All patient-identifiable information was deidentified. Only the spinal structure was retained, which was then exported as a 3D model file [in Standard Triangle Language (STL) format] for further processing. Last, the model was fabricated using a 3D printer (X1, Bambu Lab, Shanghai, China) with polylactic acid as the material.

In vivo animal experiment preparation

A 30-kg domestic pig (purchased from Chengdu Dossy Experimental Animals Co., Ltd.) was placed in the prone position (ventral recumbency) on an operation bed and secured with straps. Food was withheld for 12 hours and water was withheld for 6 hours before anesthesia to reduce gastric volume and the risk of regurgitation and aspiration. An intravenous catheter (20 gauge) was aseptically placed in the auricular vein for drug administration. All procedures were approved by the Animal Ethics Committee of West China Hospital, Sichuan University (approval no. 2021794A), and were conducted in accordance with institutional guidelines for the ethical treatment and welfare of laboratory animals. General anesthesia was induced with an intramuscular combination of azaperone (2.0 mg/kg), midazolam (0.3 mg/kg), and butorphanol (0.3 mg/kg) to achieve sedation, anxiolysis, and analgesia. After adequate sedation (10 to 15 min), vecuronium bromide [0.1 mg/kg intravenously (iv)] was administered to facilitate tracheal intubation. The pig was intubated with a 6.5- to 7.5-mm-ID endotracheal tube and ventilated mechanically. Anesthesia was maintained with desflurane at an inspired concentration of ~5% (1.0 to 1.3 minimum alveolar concentration) in 100% oxygen using a closed-circuit vaporizer system. Ventilator settings included a tidal volume of 10 ml/kg and a respiratory rate of 12 to 15 breaths/min, adjusted to maintain end-tidal carbon dioxide ($EtCO_2$) between 35 and 45 mmHg. Additional vecuronium (0.015 mg/kg iv) was administered every 30 to 40 min to maintain neuromuscular blockade as required. Physiological monitoring included electrocardiography, noninvasive blood pressure (measured every 5 min), peripheral oxygen saturation (SpO_2), $EtCO_2$, end-tidal desflurane concentration, and rectal temperature. Core body temperature was maintained between 37° and 39°C using a thermostatically controlled heating pad. Crystalloid fluid was infused intravenously at a rate of 7 ml/kg per hour. If intraoperative signs of nociception (such as tachycardia or hypertension) occurred, an additional dose of butorphanol (0.3 mg/kg) was administered. At the end of the experiment, surgical incisions were closed in layers. When the pig was still under deep anesthesia, it was euthanized humanely by intravenous injection of pentobarbital sodium (100 mg/kg), in accordance with ethical guidelines to ensure minimal suffering.

Human cadaver test preparation

A single human cadaveric specimen was used in this study to validate the performance of the robotic system. The specimen was obtained from the Department of Anatomy, West China School of Medicine, Sichuan University, through a legally authorized body donation program. To strictly protect the donor's privacy and anonymity, specific demographic details (including exact age and medical history) are not disclosed. Prescreening was performed to confirm the absence of gross pathologies or prior surgical interventions in the target lumbar region.

The specimen was preserved using a modified low-formalin embalming protocol derived from the Thiel method (*61*), which is optimized for maintaining tissue flexibility and biomechanical fidelity. Briefly, the vascular system was initially perfused via arterial infusion with a preservation solution containing <2% formaldehyde, polyols as cryoprotective agents, and balanced salts to maintain tissue hydration. After initial stabilization, the specimen was stored at −20°C. Forty-eight hours before testing, the specimen was transferred to a temperature-controlled environment for gradual thawing at room temperature. Once fully thawed and rehydrated, the specimen was secured to a radiolucent carbon fiber operating bed to facilitate intraoperative imaging. The entire experimental protocol was approved by the Ethics Committee on Biomedical Research, West China Hospital of Sichuan University (approval no. 2020554). All procedures were conducted in a controlled clinical simulation environment in accordance with institutional biosafety guidelines. The specimen was subjected to only a single freeze-thaw cycle to preserve the biomechanical fidelity of the soft tissues.

Statistical analysis

For the path-following experiments, RMSE and maximum error were calculated to evaluate tracking accuracy across repeated trials. Specifically, the optical sensing collects the position of the markers 10 times, and the mean value was used as the position data in the motion instance. All quantitative data were plotted using MATLAB (MathWorks, USA).

For stiffness characterization, force-displacement measurements were recorded and analyzed descriptively. In detail, the force data were obtained until the sensor readings were stable for at least 5 s. For task performance, 20 repeated trials were conducted on the vertebral phantom model, with the success rate defined as the ability to reach key spinal targets within a single attempt.

Owing to the limited number of biological specimens ($n = 1$ for both the human cadaveric specimen and the in vivo animal model), formal statistical hypothesis testing was not performed for these components of the study. Instead, the results are presented as feasibility assessments and qualitative validations. Procedural durations were extracted post hoc via retrospective video analysis, and intraoperative blood loss was clinically estimated by the operating surgeon on the basis of bleeding duration and anatomical site.

Supplementary Materials

The PDF file includes:
Supplementary Results
Tables S1 to S4
Figs. S1 to S12
Legends for movies S1 to S5

Other Supplementary Material for this manuscript includes the following:
Movies S1 to S5
Data file S1
MDAR Reproducibility Checklist
ARRIVE Checklist

REFERENCES AND NOTES

1. M. Gallucci, N. Limbucci, A. Paonessa, A. Splendiani, Degenerative disease of the spine. *Neuroimaging Clin. N. Am.* **17**, 87–103 (2007).
2. V. M. Ravindra, S. S. Senglaub, A. Rattani, M. C. Dewan, R. Härtl, E. Bisson, K. B. Park, M. G. Shrime, Degenerative lumbar spine disease: Estimating global incidence and worldwide volume. *Global Spine J.* **8**, 784–794 (2018).
3. M. Cheng, Y. Xue, M. Cui, X. Zeng, C. Yang, F. Ding, L. Xie, Global, regional, and national burden of low back pain: Findings from the Global Burden of Disease Study 2021 and projections to 2050. *Spine* **50**, E128–E139 (2025).
4. S. H. Farber, B. Valenzuela Cecchi, L. K. O'Neill, K. M. Chapple, J. J. Zhou, N. Alan, T. C. Gooldy, J. D. DiDomenico, L. A. Snyder, J. D. Turner, J. S. Uribe, Complications associated with single-position prone lateral lumbar inter-body fusion: A systematic review and pooled analysis. *J. Neurosurg. Spine* **39**, 380–386 (2023).
5. T. A. Gionis, E. Groteke, Spinal decompression. *Orthop. Technol. Rev.* **5**, 36–39 (2003).
6. H. Yoshihara, Indirect decompression in spinal surgery. *J. Clin. Neurosci.* **44**, 63–68 (2017).
7. T. Karlsson, P. Försth, P. Öhagen, K. Michaëlsson, B. Sandén, Decompression alone or decompression with fusion for lumbar spinal stenosis: Five-year clinical results from a randomized clinical trial. *BoneJoint J.* **106-B**, 705–712 (2024).
8. F.-Y. Tsuang, Y.-L. Hsu, T.-Y. Chou, C. L. Chai, Long-term reoperation after decompression with versus without fusion among patients with degenerative lumbar spinal stenosis: A systematic review and meta-analysis. *Spine J.* **25**, 1096–1107 (2025).
9. G. M. Overdevest, W. Jacobs, C. Vleggeert-Lankamp, C. Thomé, R. Gunzburg, W. Peul, Effectiveness of posterior decompression techniques compared with conventional laminectomy for lumbar stenosis. *Eur. Spine J.* **23**, 2244–2263 (2015).
10. R. J. Mobbs, K. Phan, G. Malham, K. Seex, P. J. Rao, Lumbar interbody fusion: Techniques, indications and comparison of interbody fusion options including PLIF, TLIF, MI-TLIF, OLIF/ATP, LLIF and ALIF. *J. Spine Surg.* **1**, 2–18 (2015).
11. Y.-H. Huang, C.-Y. Ou, Significant blood loss in lumbar fusion surgery for degenerative spine. *World Neurosurg.* **84**, 780–785 (2015).
12. A. S. Hilibrand, M. Robbins, Adjacent segment degeneration and adjacent segment disease: The consequences of spinal fusion? *Spine J.* **4**, S190–S194 (2004).
13. Z. Pennington, S. J. Sundar, D. Lubelski, M. D. Alvin, E. C. Benzel, T. E. Mroz, Cost and quality of life outcome analysis of postoperative infections after posterior lumbar decompression and fusion. *J. Clin. Neurosci.* **68**, 105–110 (2019).
14. J. Allain, T. Dufour, Anterior lumbar fusion techniques: ALIF, OLIF, DLIF, LLIF, IXLIF. *Orthop. Traumatol. Surg. Res.* **106**, S149–S157 (2020).
15. K. Phan, M. Maharaj, Y. Assem, R. J. Mobbs, Review of early clinical results and complications associated with oblique lumbar interbody fusion (OLIF). *J. Clin. Neurosci.* **31**, 23–29 (2016).
16. H.-F. Zhu, X. Q. Fang, F. D. Zhao, J. F. Zhang, X. Zhao, Z. J. Hu, S. W. Fan, Comparison of oblique lateral interbody fusion (OLIF) and minimally invasive transforaminal lumbar interbody fusion (MI-TLIF) for treatment of lumbar degeneration disease: A prospective cohort study. *Spine* **47**, E233–E242 (2022).
17. D. S. Xu, C. T. Walker, J. Godzik, J. D. Turner, W. Smith, J. S. Uribe, Minimally invasive anterior, lateral, and oblique lumbar interbody fusion: A literature review. *Ann. Transl. Med.* **6**, 104 (2018).
18. N. R. Khan, A. J. Clark, S. L. Lee, G. T. Venable, N. B. Rossi, K. T. Foley, Surgical outcomes for minimally invasive vs open transforaminal lumbar interbody fusion: An updated systematic review and meta-analysis. *Neurosurgery* **77**, 847–874 (2015).
19. J. Zhang, T. F. Liu, H. Shan, Z. Y. Wan, Z. Wang, O. Viswanath, A. Paladini, G. Varrassi, H. Q. Wang, Decompression using minimally invasive surgery for lumbar spinal stenosis associated with degenerative spondylolisthesis: A review. *Pain Ther.* **10**, 941–959 (2021).
20. G. Choi, C. S. Pophale, B. Patel, P. Uniyal, Endoscopic spine surgery. *J. Korean Neurosurg. Soc.* **60**, 485–497 (2017).
21. A. Boaro, B. Mahadik, A. Petrillo, F. Siddi, S. Devi, S. Chawla, A. M. Abunimer, A. Feletti, A. Fiorindi, P. Longatti, F. Sala, T. R. Smith, R. A. Mekary, Efficacy and safety of flexible versus rigid endoscopic third ventriculostomy in pediatric and adult populations: A systematic review and meta-analysis. *Neurosurg. Rev.* **45**, 199–216 (2022).
22. B. Carl, M. Bopp, B. Saß, C. Nimsky, Microscope-based augmented reality in degenerative spine surgery: Initial experience. *World Neurosurg.* **128**, e541–e551 (2019).
23. A. G. Bishop, T. L. Uhl, J. B. Zwischenberger, S. L. Meyerson, Prevalence and impact of musculoskeletal pain due to operating among surgical trainees. *J. Surg. Educ.* **80**, 676–681 (2023).
24. B. Z. Chin, J. H. Yong, E. Wang, S. I. Sim, S. Lin, P. H. Wu, H. W. D. Hey, Full-endoscopic versus microscopic spinal decompression for lumbar spinal stenosis: A systematic review & meta-analysis. *Spine J.* **24**, 1022–1033 (2024).
25. C.-C. Ko, P.-H. Lee, J.-S. Lee, K.-Z. Lee, Spinal decompression surgery may alleviate vasopressor-induced spinal hemorrhage and extravasation during acute cervical spinal cord injury in rats. *Spine J.* **24**, 519–533 (2024).
26. R. Härtl, K. S. Lam, J. Wang, A. Korge, F. Kandziora, L. Audigé, Worldwide survey on the use of navigation in spine surgery. *World Neurosurg.* **79**, 162–172 (2013).
27. A. Picciariello, A. Annicchiarico, G. Gallo, A. Dezi, U. Grossi, Evaluation of the da Vinci single-port system in colorectal cancer surgery: A scoping review. *Updates Surg.* **76**, 2515–2520 (2024).
28. F. Celotto, N. Ramacciotti, A. Mangano, G. Danieli, F. Pinto, P. Lopez, A. Ducas, J. Cassiani, L. Morelli, G. Spolverato, F. M. Bianco, Da Vinci single-port robotic system current application and future perspective in general surgery: A scoping review. *Surg. Endosc.* **38**, 4814–4830 (2024).
29. K. Bach, J. Ford, R. Foley, J. Januszewski, R. Murtagh, S. Decker, J. S. Uribe, Morphometric analysis of lumbar intervertebral disc height: An imaging study. *World Neurosurg.* **124**, e106–e118 (2019).
30. M. H. Lee, H. J. Jang, B. J. Moon, K. H. Kim, D. K. Chin, K. S. Kim, J.-Y. Park, Comparative outcomes of biportal endoscopic decompression, conventional subtotal laminectomy, and minimally invasive transforaminal lumbar interbody fusion for lumbar central stenosis. *Neurospine* **21**, 1178–1189 (2024).
31. K. J. Nicholson, B. A. Winkelstein, "Nerve and nerve root biomechanics" in *Neural Tissue Biomechanics*, L. E. Bilston, Ed., vol. 3 of *Studies in Mechanobiology, Tissue Engineering, and Biomaterials* (Springer, 2010), pp. 203–229.
32. R. Li, J. Ni, X. Li, B. Wu, B. Li, R. P. Su, S. Xue, Y. An, G. J. Wu, Functional outcomes after 'SHURUI' single-port robot-assisted pyeloplasty for uretero pelvic junction obstruction: Single-centre experience. *Int. J. Med. Robot.* **21**, e70056 (2025).
33. F. Wang, H. Wang, J. Luo, X. Kang, H. Yu, H. Lu, Y. Dong, X. Jia, FIORA: A flexible tendon-driven continuum manipulator for laparoscopic surgery. *IEEE Robot. Autom. Lett.* **7**, 1166–1173 (2022).
34. T. Kato, I. Okumura, S.-E. Song, A. J. Golby, N. Hata, Tendon-driven continuum robot for endoscopic surgery: Preclinical development and validation of a tension propagation model. *IEEE/ASME Trans. Mechatron.* **20**, 2252–2263 (2014).
35. J. Davy, T. P. Dean, N. J. Greenidge, B. Calmé, P. Lloyd, J. H. Chandler, P. Valdastri, Magnetic fluid-driven vine robots for minimally invasive tissue biopsy sampling. *Adv. Intell. Syst.* **7**, 2400827 (2025).
36. M. Ghevondyan, M. Davtyan, M. Aghayan, Dielectric elastomer actuators: Medical applications review. *Discov. Mater.* **5**, 43 (2025).
37. X. Wang, W. Kang, X. Liang, K. Ban, J. Liu, J. Zhang, A magnetic catheter with force sensing capability toward interventional surgery. *IEEE Robot. Autom. Lett.* **9**, 10375–10382 (2024).
38. K. Price, J. Peine, M. Mencattelli, Y. Chitalia, D. Pu, T. Looi, S. Stone, J. Drake, P. E. Dupont, Using robotics to move a neurosurgeon's hands to the tip of their endoscope. *Sci. Robot.* **8**, eadg6042 (2023).
39. M. F. Rox, D. S. Ropella, R. J. Hendrick, E. Blum, R. P. Naftel, H. C. Bow, S. D. Herrell, K. D. Weaver, L. B. Chambless, R. J. Webster, Mechatronic design of a two-arm concentric tube robot system for rigid neuroendoscopy. *IEEE/ASME Trans. Mechatron.* **25**, 1432–1443 (2020).
40. T. E. Ertop, J. F. d'Almeida, E. Amanov, J. Shrand, N. Nimmagadda, S. Setia, "Towards suturing from within the urethra using concentric tube robots: First experiences in biological tissues" in *2022 International Symposium on Medical Robotics (ISMR)* (IEEE, 2022), pp. 1–5.
41. J. Tian, T. Wang, X. Fang, Z. Shi, Design, fabrication and modeling analysis of a spiral support structure with superelastic Ni-Ti shape memory alloy for continuum robot. *Smart Mater. Struct.* **29**, 045007 (2020).
42. M. Tummers, F. Boyer, V. Lebastard, A. Offerman, J. Troccaz, B. Rosa, M. T. Chikhaoui, Continuum concentric push-pull robots: A Cosserat rod model. *Int. J. Robot. Res.* **44**, 02783649241263366 (2024).
43. J. A. Childs, C. Rucker, A kinetostatic model for concentric push-pull robots. *IEEE Trans. Robot.* **40**, 554–572 (2024).
44. T. L. Bruns, A. A. Remirez, M. A. Emerson, R. A. Lathrop, A. W. Mahoney, H. B. Gilbert, C. L. Liu, P. T. Russell, R. F. Labadie, K. D. Weaver, R. J. Webster III, A modular, multi-arm concentric tube robot system with application to transnasal surgery for orbital tumors. *Int. J. Robot. Res.* **40**, 521–533 (2021).
45. A. R. Lanfranco, A. E. Castellanos, J. P. Desai, W. C. Meyers, Robotic surgery: A current perspective. *Ann. Surg.* **239**, 14–21 (2004).
46. M. J. Mack, Minimally invasive and robotic surgery. *JAMA* **285**, 568–572 (2001).
47. M. Diana, J. Marescaux, Robotic surgery. *Br. J. Surg.* **102**, e15–e28 (2015).

48. G. Fang, Z.-x. Wu, Y. Fan, J. Fu, M. Gong, W. Cui, M. Wu, H. Wang, L. Zheng, H. Sang, G. Pei, Clinical application of Renaissance spine robot assisted system in spinal disease. *Chin. J. Orthop. Trauma* **2017**, 299–303 (2017).
49. M. Bhimreddy, A. M. Hersh, K. Jiang, C. Weber-Levine, A. D. Davidar, A. K. Menta, B. F. Judy, D. Lubelski, A. Bydon, J. Weingart, N. Theodore, Accuracy of pedicle screw placement using the ExcelsiusGPS robotic navigation platform: An analysis of 728 screws. *Int. J. Spine Surg.* **18**, 712–720 (2024).
50. E. Summerside, J. Heller, J. Glenn, B. McCormack, P. P. M. Menchetti, "Tissue sparing posterior fixation as a treatment option for degenerative disc disease" in *Cervical Spine: Minimally Invasive and Open Surgery*, P. P. M. Menchetti, Ed. (Springer, ed. 2, 2022), pp. 231–245.
51. I. Busscher, J. J. Ploegmakers, G. J. Verkerke, A. G. Veldhuizen, Comparative anatomical dimensions of the complete human and porcine spine. *Eur. Spine J.* **19**, 1104–1114 (2010).
52. Q. He, J. Mei, N. Yao, W. Qian, H. Yin, X. Sun, Clinical results of oblique lateral interbody fusion OLIF technique compared with conventional lumbar posterior laminar decompression for lumbar spinal stenosis. *Am J. Biomed. Sci. Res.* **43**, 34497–34503 (2022).
53. Q. Huang, W. Zhu, P. Cui, S. Wang, D. Han, P. Wang, S. Lu, A retrospective cohort study comparing perioperative clinical outcomes and radiographic results between patients undergoing TLIF and OLIF surgeries. *BMC Surg.* **25**, 188 (2025).
54. J. Wang, X. Yang, P. Li, S. Song, L. Liu, M. Q. H. Meng, Design of a multi-arm concentric-tube robot system for transnasal surgery. *Med. Biol. Eng. Comput.* **58**, 497–508 (2020).
55. T. Vandebroek, M. Ourak, C. Gruijthuijsen, A. Javaux, J. Legrand, T. Vercauteren, "Macro-micro multi-arm robot for single-port access surgery" in *2019 IEEE/RSJ International Conference on Intelligent Robots and Systems (IROS)* (IEEE, 2019), pp. 425–432.
56. R. J. Webster III, B. A. Jones, Design and kinematic modeling of constant curvature continuum robots: A review. *Int. J. Robot. Res.* **29**, 1661–1683 (2010).
57. Y. Li, D. H. Myszka, A. Murray, The kinematics of constant curvature continuum robots through three segments. *IEEE Robot. Autom. Lett.* **8**, 7631–7638 (2023).
58. L. Hou, X. Zhao, T. Chen, Y. Zhang, Q. Ling, B. Tao, A sensing strategy combining kinematic model with FBG sensors for continuum robots. *IEEE Trans. Instrum. Meas.* **74**, 1–11 (2025).
59. B. Ahmad, P. A. Floor, I. Farup, C. F. Andersen, Single-image-based 3D reconstruction of endoscopic images. *J. Imaging* **10**, 82 (2024).
60. K. Oliver-Butler, J. A. Childs, A. Daniel, D. C. Rucker, Concentric push–pull robots: Planar modeling and design. *IEEE Trans. Robot.* **38**, 1186–1200 (2022).
61. W. Thiel, Supplement to the conservation of an entire cadaver according to W. Thiel. *Ann. Anat.* **184**, 267–269 (2002).

Acknowledgments
Funding: This work was funded by the 1·3·5 project for disciplines of excellence, West China Hospital, Sichuan University (ZYYC21004); the Postdoctor Research Fund of West China Hospital, Sichuan University (2025HXBH057); the Sichuan Provincial Natural Science Foundation (2026NSFSC1240); and the Science and Technology Bureau of Chengdu (2026YF1100034HZ). **Author contributions:** Q.Z. conceived the robotic system idea, designed the instruments, and organized this paper. X.W. proposed the clinical demand and led all the medical-related experiments. R.Z. and X.Z. designed the mechanical structure and the electronic part of the system, respectively. D.P. supported the setup of all medical-related experimental environments. B.L., T.L., S.S., H. Zhou, and Y.C. worked in clinical trials and preparation for the experiments. H.K.C. organized the structure of this manuscript, designed the robot-related experiments, and polished the text. H. Zheng and P.Z. worked in experiments and writing. J.Z. supervised and instructed all the trials. K.L. supported the whole project and revised this manuscript. **Competing interests:** The authors declare that they have no competing interests. **Data, code, and materials availability:** All data needed to support the conclusions of this manuscript are included in the main text or Supplementary Materials. The data and code for this study have been deposited in the Dryad database (DOI: 10.5061/dryad.08kprr5gm). No new materials were developed in this study.

Submitted 15 October 2025
Accepted 28 April 2026
Published 27 May 2026
10.1126/scirobotics.adu0590

Science Robotics

A minimally invasive robotic spinal surgical system for anterior lumbar nerve decompression

Qingxiang Zhao, Xiandi Wang, Xin Zhong, Runfeng Zhu, Peizhi Zhou, Dan Pu, Baitao Lin, Tao Li, Shiyuan Sui, Haonan Zhou, Yuxi Cheng, Hao Zheng, Henry K. Chu, Jiancheng Zeng, and Kang Li

Sci. Robot. **11** (114), eadu0590. DOI: 10.1126/scirobotics.adu0590